**Atmospheric
Measurement
Techniques
Discussions**

Seven years of global retrieval of cloud properties using space-borne data of GOME-1

L. Lelli[1], A. A. Kokhanovsky[1], V. V. Rozanov[1], M. Vountas[1], A. M. Sayer[2], and J. P. Burrows[1]

[1]Institute of Environmental Physics and Remote Sensing, University of Bremen, Otto-Hahn-Allee 1, 28334 Bremen, Germany
[2]Goddard Earth Sciences Technology And Research (GESTAR), NASA Goddard Space Flight Center, Greenbelt, MD 20771, USA

Correspondence to: L. Lelli (luca@iup.physik.uni-bremen.de)

AMTD

4, 4991–5035, 2011

Global cloud properties from GOME-1

L. Lelli et al.

Title Page

Abstract	Introduction
Conclusions	References
Tables	Figures

| ◄◄ | ►► |
| ◄ | ► |

Back | Close

Full Screen / Esc

Printer-friendly Version

Interactive Discussion

Abstract

We present a global and regional multi-annual (1996–2002) analysis of cloud properties (spherical albedo, optical thickness and top height) derived using measurements from the GOME-1 instrument onboard the ESA ERS-2 space platform. We focus on cloud top height (CTH), which is obtained from top-of-atmosphere backscattered solar light measurements in the O_2 A-band using the Semi-Analytical CloUd Retrieval Algorithm SACURA. The physical framework relies on the asymptotic equations of radiative transfer. The dataset has been validated against independent ground- and satellite-based retrievals and is aimed to support ozone and trace-gases studies as well as to create a robust long-term climatology together with SCIAMACHY and GOME-2 ensuing retrievals. We observed the El Niño Southern Oscillation anomaly in the 1997–1998 record through CTH values over Pacific Ocean. Analytical forms of probability density functions of seasonal CTH are proposed for parameterizations in climate modeling. The global average CTH as derived from GOME-1 is 7.0 ± 1.18 km.

1 Introduction

Clouds play an important role in the Earth climate system (Stephens, 2005). The amount of radiation reflected by the Earth-atmosphere system into outer space depends not only on the cloud cover and the total amount of condensed water in the atmosphere but, also on the size of droplets and their thermodynamic state. The information about microphysical properties, cloud top height and spatial distributions of terrestrial clouds on a global scale can be obtained optimally with satellite remote sensing systems. The amount of reflected solar light depends both on geometrical and microphysical characteristics of clouds. In particular, it is often assumed that clouds can be represented by homogeneous and (in horizontal direction) infinitely extended plane-parallel slabs. The range of applicability of such an assumption for real clouds is limited, because 3-D effects are not taken into account. However some properties can still be derived and valuable information can be retrieved.

Though the main scientific objective of GOME (Global Ozone Monitoring Experiment, Burrows et al., 1999) is the retrieval of trace gases, its measurements are also relevant for the study of cloud parameters. GOME-1 is a space-borne spectrometer that flies on ERS-2 since April 1995 and measures reflected solar radiation in the wavelength range between 237 and 794 nm at moderate high spectral resolution of 0.2 to 0.4 nm (see Table 1).

Clouds affect the path of light through the atmosphere and therefore change the interpretation of the depth of an absorption band. They act as reflectors and absorbers and their influence can be summarized in three components: firstly they shield the troposphere, hiding the gas columns below; secondly they enhance the absorption above and inside a cloud (due to light path enhancement), yielding an increased band depth; finally they cause multiple scattering, as photons travel inside. Hence the properties to be known are cloud albedo, optical thickness and top height.

The aim of this paper is to describe the retrieval of such properties with SNGome (SACURA – Semi-Analytical CloUd Retrieval Algorithm – Next Generation for GOME) and assess the quality of the dataset through validation and comparison with other algorithms, based on different physical approaches. The main focus is on cloud top height. The structure of the paper is as follows. In Sect. 2 the algorithm is described. The solution of the forward and inverse problem is sketched as well as the extension to global processing. Section 3 is devoted to validation, both synthetic error analysis and against radar measurements and other retrieval techniques. In Sect. 4 we show results and global cloud patterns. In the final section we draw some conclusions.

2   SNGome algorithm description

It has been extensively proven that cloud top height can be retrieved from measurements in the oxygen A-band (758–778 nm) (Yamamoto and Wark, 1961; Saiedy et al., 1967; Fischer and Grassl, 1991; Kuze and Chance, 1994; Kuji and Nakajima, 2002; Rozanov and Kokhanovsky, 2004). When a cloud is idealized as a perfect reflector,

every photon striking to the cloud top will be scattered back and will not be absorbed by O_2 molecules within or below the cloud. So the depth of the absorption line decreases as the cloud altitude increases, because most of the oxygen is located under the clouds.

In reality, the assumption of a cloud as a Lambertian diffuser with zero transmittance and fixed single scattering albedo leads to the underestimation of height, because smaller top-of-atmosphere (TOA) reflectances are misinterpreted as lower cloud layers (firstly remarked by Saiedy et al., 1967). Moreover, it has been shown that the sole retrieval of top height will be biased low if no attempt is made to retrieve the geometrical thickness and its value will be closer to the altitude of the middle of the cloud (Ferlay et al., 2010).

The SNGome algorithm is based on SACURA (Kokhanovsky et al., 2003; Rozanov and Kokhanovsky, 2004). It was originally developed at IUP Bremen for the application to SCIAMACHY measurements (Gottwald and Bovensmann, 2010; Burrows et al., 2011; Kokhanovsky et al., 2011a). It consists of two parts: a forward analytical parametrization of the cloud TOA reflection function and a numerical minimization for the retrieval. Extensive description can be found in Kokhanovsky et al. (2003); Rozanov and Kokhanovsky (2004); Kokhanovsky and Rozanov (2004); Kokhanovsky and Nauss (2006).

Due to the coarse GOME-1 spatial resolution, two corrections are introduced to address the issue of broken cloudiness. First, it has been shown that horizontal photon transport can be neglected and 1-D calculations suffice (Kokhanovsky et al., 2007a). Hence partially cloudy scenes are scaled to fully cloudy cases with the Independent Pixel Approximation (IPA) (Marshak et al., 1995) and the cloud TOA reflectance R_{cl} is calculated from

$$R_{mes} = c_f R_{cl} + (1 - c_f) R_s \qquad (1)$$

The value of cloud fraction c_f, defined as the fraction of the GOME-1 pixel occupied by a cloud, is delivered by DLR (Deutsches Zentrum für Luft- und Raumfahrt) in bundle

with the GOME-1 radiances and is based on the analysis of Polarization Measuring Device (PMD) records (Loyola and Ruppert, 1998; Loyola, 2004). The clear sky reflectance R_s is substituted by a Minimum Lambert-Equivalent Reflectivity (MLER) value taken from the global database Tropospheric Emission Monitoring Internet Service (TEMIS, Koelemeijer et al. (2003), see Table 5). This climatological value has been derived from 5.5 years of GOME-1 observations, therefore ensuring consistency. The TEMIS sub-pixels are co-located with trigonometrical considerations (see Eqs. 1 and 2 in Kokhanovsky et al., 2007c) and averaged.

Secondly, the influence of the surface reflection on the top-of-atmosphere reflection of the cloudy scene, assuming that the surface is Lambertian with albedo A, is taken into account with (see Eq. 54 in Kokhanovsky et al., 2003)

$$R_{TOA} = R_\infty - t\, K_0(\mu)K_0(\mu_0) + \frac{A\, t^2\, K_0(\mu)K_0(\mu_0)}{1 - A\,(1-t)} \tag{2}$$

where t is the cloud transmissivity, $K_0(\mu)$ and $K_0(\mu_0)$ are the escape functions, μ and μ_0 the cosines of viewing and solar zenith angles and R_∞ the reflection function of an infinite layer, respectively. Arguments in R_∞ and R_{mes} are omitted for simplicity. The escape function can be approximated as

$$K_0(\mu) = \frac{3}{7}(1+2\mu) \tag{3}$$

with an accuracy of 2 % at $\mu \geqslant 0.2$ (Kokhanovsky, 2006). The value of t is related to the cloud optical thickness (COT) τ via

$$t = \frac{1}{\alpha + 0.75\, \tau\,(1-g)}. \tag{4}$$

The asymmetry parameter g depends on the chosen phase function. We will assume that $g = 0.859$ (i.e., water clouds, Kokhanovsky, 2006). The parameter α is almost independent of microphysics of clouds and is set equal to 1.07 (Kokhanovsky, 2006).

Title Page

Abstract | Introduction

Conclusions | References

Tables | Figures

◄ | ►

◄ | ►

Back | Close

Full Screen / Esc

Printer-friendly Version

Interactive Discussion

The optical thickness τ is then calculated from the continuum outside the absorption, at wavelength 758 nm, where almost no sensitivity to cloud top height is expected. Then it follows from Eqs. (2) and (4):

$$\tau = \frac{1 - A - D\ (\beta - A)(\alpha - 1)}{0.75\ D\ (1 - A)(1 - g)}, \qquad D = \frac{R_\infty - R_{TOA}}{K_0(\mu)K_0(\mu_0)}. \tag{5}$$

5 where $\beta = \frac{\alpha}{\alpha - 1}$. This technique, used also in King (1987), applies to clouds with $\tau > 5$.

The values of geometrical cloud height h and thickness l are derived from measurements around the oxygen absorption centered at 761 nm, with the nominal GOME-1 spectral resolution and sampling (67 spectral points were used). In this case, the modeled reflectance R_{TOA} is modified accounting for both gaseous absorption and multi-10 ple light scattering inside and below the cloud. Exhaustive formulae can be found in Rozanov and Kokhanovsky (2004).

The retrieval block of SNGome relies on the minimization between the forward modeled TOA reflectances and the reflectances observed in the wavelength range 758–772 nm. It is assumed that the reflection function R can be expanded in the Taylor 15 series around the a-priori value of the cloud top height h_0

$$R(h) = R(h_0) + \sum_{i}^{\infty} a_i(h - h_0)^i \qquad \text{and} \qquad a_i = \frac{R^{(i)}(h_0)}{i!} \tag{6}$$

with $R^{(i)}(h_0)$ being the i-th derivative of R corresponding to cloud top height h_0. It was found that the function $R(h)$ is close to a linear one in a broad interval of the argument change (Rozanov and Kokhanovsky, 2004). Therefore, neglecting nonlinear terms in 20 Eq. (6), it follows

$$R(h) = R(h_0) + R'(h_0)(h - h_0) \qquad \text{and} \qquad R'(h_0) = \frac{dR}{dh}\bigg|_{h = h_0}. \tag{7}$$

Having fixed the initial value of h_0 equal to 1.0 km, a value typical for low level clouds, the actual cloud top height h is calculated minimizing the cost function

$$\mathbf{F} = \|R_{\mathrm{cl}} - R(h_0) - R'(h_0)(h - h_0)\|^2. \tag{8}$$

The retrieval of the pair (h, l) is accomplished writing a vectorial form of the above equation and performing a two-parameter minimization (Rozanov and Kokhanovsky, 2004), where R_{cl} is the TOA reflectance calculated with Eq. (1). The correlated k-distribution accounts for the high-frequency oscillations of the oxygen molecular absorption coefficients K_{abs}. The temperature and pressure dependence of K_{abs} for a given location of measurements is accounted for using the standard atmosphere model (Brühl and Crutzen, 1993).

Finally, the cloud spherical albedo r is calculated with the aid of Eq. (4), taking into account that $t = 1 - r$, if one neglects absorption processes. The error for r has been estimated smaller than 10 % at $\tau \gtrsim 6$ and below 3 % at $\tau \gtrsim 10$. The technique has been validated by comparing retrieved values of r with airborne measurements, showing remarkable agreement (Kokhanovsky et al., 2007b).

For global processing we employ the digital elevation model STRM30 (Earth Resources Observation and Science (EROS, USGS) Center, 2000). The fundamental sample spacing of 3 arc-second in latitude and longitude (≈ 90 m at equator) has been down-sampled to 0.5 arc-minute in both coordinates (≈ 1 km at equator).

In summary, the strengths of the algorithm are the analytical forward parametrization of the TOA reflectances in the wavelength range of the oxygen A-band (but suitable to the broader range 0.4–2.4 µm) for clouds with $\tau > 5$ and solar zenith angles $\leqslant 75°$, the inclusion of molecular, aerosol scattering in clear sky condition and multiple scattering inside the cloud. In this way we avoid the common look-up-table approach.

3   Validation

3.1   Synthetic error analysis

The theoretical error investigation has been carried out generating forward spectra with the radiative transfer software package SCIATRAN (v. 3.1, Rozanov et al., 2011)
and ingesting them in SNGome. In the first case study, a single layered water cloud of fixed geometrical thickness 1 km and optical thickness in the range [5–50] has been moved in the height range [2–16] km. The phase function of water particles (of effective radius 6 μm and Deirmendjian's cloud C1 droplet distribution (Deirmendjian, 1969)) is assumed to be the same through the cloud. The underlying surface has been assumed
black. The solar zenith angle has been set equal to 60° and viewing zenith angle equal to 0°. The absolute error of the retrieved top altitude, defined as

$$\Delta = CTH_{retrieved} - CTH_{true}$$

is shown in Fig. 1. The error is in the expected value range (±0.5 km), in line with pre-
vious findings (Rozanov and Kokhanovsky, 2004), where the authors already pointed out the decreased sensitivity to oxygen absorption for high and thin clouds. However such clouds cannot be detected anyway by GOME-1, as reported in Rozanov et al. (2006). Moreover GOME-1 is a UV-VIS instrument, lacking spectral coverage in the short-wave IR. This limitation implies the lack of information on the cloud phase func-
tion for the retrievals beforehand, because only very weak absorption by water takes
place in the oxygen A-band, hence no cloud particles size can be inferred. For this reason errors are introduced if the phase function will be only guessed and solar illu-
mination geometry varies appreciably. Yet, in order to test the algorithm under realistic operational conditions, the choice has been to maintain a slight difference between the asymmetry parameters g in Eq. (4) (and therefore between the phase functions) used
in the forward ($g = 0.846$) and inverse ($g = 0.859$) problem. The error depicted in Fig. 2 discloses this effect as the solar zenith angle approaches the value ranges [5°–10°] and [42°–44°]. Due to the geometry of the experiment, these angles correspond to glory

Title Page

Abstract | Introduction

Conclusions | References

Tables | Figures

|◄ | ►|

◄ | ►

Back | Close

Full Screen / Esc

Printer-friendly Version

Interactive Discussion

and rainbow regions, where the chosen phase functions differ the most. The same effect is mirrored for cloud optical thickness retrieval, whose relative error is shown in Fig. 3.

3.2 Comparison with other datasets

In order to test the soundness of SNGome cloud top heights retrievals, we compare the results with two different and independent space-based algorithms and ground-based measurements. The first dataset is GRAPE (Global Retrieval of ATSR Cloud Parameters and Evaluation) (Poulsen et al., 2011; Sayer et al., 2011), relying on the ORAC (Oxford and RAL – Rutherford Appleton Laboratory – Aerosols and Clouds) re-trieval engine. The data are made freely available via the British Atmospheric Data Center (http://badc.nerc.ac.uk/data/grape/). Both dataset are cross-validated against ground-based radar measurements from four different facilities. The second algorithm is ROCINN, operationally deployed by DLR (Loyola et al., 2007). The basic idea be-hind this comparison is to gain insight on the strength and weakness of each technique. They rely on three different physical principles. GRAPE is based on the passive ther-mal measurements of ATSR-2, while ground-based data rely on a combination of active measurements such as cloud radar (CR), micro-pulse lidar (L), millimeter-wave cloud radar (M) and ceilometer (C) (see Table 3). ROCINN is based on the O_2 A-band tech-nique but with a LUTs and neural network approach. Clearly different parts of the cloud are sensed and the intercomparison is not straightforward.

3.2.1 GRAPE and Radar

The Along-Track Scanning Radiometer (ATSR-2)(Stricker et al., 1995) is a dual-view infrared sounder onboard the ESA ERS-2 space platform, being the natural choice for comparison with GOME-1, since no temporal lag between the two instruments and the same cloud scene is assumed. Even so, the limited across-nadir swath ($\approx$500 km) of the ATSR-2 reduces the number of co-registered retrievals of SNGome and the

off-nadir pixels of GOME-1 cannot be used, resulting in a decreased spatial coverage. The radar facilities description used in this evaluation is given in Table 3.

The physical principle the GRAPE algorithm is based on is the cloud infrared (IR) brightness temperature as observed by ATSR-2 (Poulsen et al., 2011). Clouds located higher up in atmosphere are generally colder. Local temperature profiles are used to match the derived cloud-top-temperature with the equivalent cloud altitude. The main assumptions in the GRAPE retrieval scheme are:

– Look-Up-Tables of atmospheric transmittance and reflectance (DISORT as radiative transfer code and MODTRAN for the gaseous absorption part)

– Lambertian surface (MODIS albedo product for 2002)

– cloud model as single layered

– pressure, temperature and H_2O profiles according to ECMWF (ERA-40 dataset).

More details on the algorithm can be found in Poulsen et al. (2011), while an evaluation of the data, and the criteria for data selection, are given in Sayer et al. (2011). SNGome data selection and properties are as follows:

– the ground-based site is inside the GOME-1 pixel at a maximum of half of its size

– the quality flag of SNGome is 5 (best convergence)

– no restriction on fractional cloud cover has been made. Hence cloud fraction is in the range [0.17–1] for the investigated scenes.

The scenes are additionally subset as "deep clouds" if the top of the cloud is higher than 3 km and vertical extent of the cloud greater than half of its height, whereas "shallow" clouds otherwise. This distinction has been made in view of the fact that vertically heterogeneous clouds might occur, in contrast to single-layered homogenous ones. 33 co-registered overpasses have been selected for the deep cloud scenario and plotted

in Fig. 4. 11 overpasses have been matched for the shallow cloud scenario and plotted in Fig. 5. The statistics are shown in Table 4.

Firstly the findings confirm what has been already explained by Sherwood et al. (2004); Rozanov et al. (2006); Sayer et al. (2011). Infrared sounding techniques are affected by a systematic bias, as a consequence of the assumption that a cloud is a black body radiator in the IR, for that reason the profile matches at higher temperature, placing the cloud too low. This effect can be seen in both cloud field types. Especially for deep (likely multi-layered) clouds the simultaneous retrieval of top and bottom altitude seems to be more suitable, despite the fact that a single layered cloudiness is assumed in the model. It has been shown that inference of both parameters, using the full spectral informations in the A-band (Rozanov et al., 2004) or multi-angular measurements (Ferlay et al., 2010), mitigates this uncertainty.

Secondly, because of the asymptotic relations SNGome is based on, the accuracy of the retrieval of cloud top height depends on the optical thickness. The theory is valid for clouds optically thicker than 5. If a thin cloud (COT $\leqslant$ 5) is encountered, the derived cloud top height will be placed higher, because of its dependency on COT. This is indeed the case in Fig. 5. The COT values (not shown here) of GRAPE are smaller than of SNGome.

Overall, where the satellite retrievals deviate from radar top height, they exhibit opposite signs, backing the idea of synergistic use of oxygen A-band and infrared techniques. Therefore, the profiling capabilities of the former together with the radiative sounding of the latter can result in value-added datasets and should not be rejected for future instruments' design.

3.2.2 ROCINN

The Retrieval of Cloud Information using Neural Network (ROCINN) algorithm (Loyola, 2004; Loyola et al., 2007) uses the oxygen absorption band and a combination of LUTs of forward reflectivities and neural network to deliver cloud top height (pressure) and albedo, with the same cloud fraction used in SNGome and calculated with OCRA

(Optical Cloud Recognition Algorithm, (Loyola and Ruppert, 1998; Loyola et al., 2007)). We compare the same dataset described in the work of Rozanov et al. (2006). Four separated GOME-1 orbits (15453, 16910, 18366, 19537) were selected, which are considered to be representative of climatological and geometrical illumination conditions. Such orbits have been operated in enhanced narrow observation mode (i.e., ground pixel size $80 \times 40 \, \mathrm{km}^2$), thus the results can be extended to instruments with equivalent spatial resolution as GOME-2 ($80 \times 40 \, \mathrm{km}^2$) and SCIAMACHY ($30 \times 60 \, \mathrm{km}^2$).

Figure 6 shows the comparison for the orbit 16910 (date 15 July 1998). This orbit is geographically situated over Europe and the Benguela region, the basin facing west Africa. In the upper panel the CTHs differences between SNGome and ROCINN version 4 (actual version) are plotted, together with the co-registered values of CTH from ATSR (black squares). In the lower panel the difference between OCRA cloud fraction and ATSR cloud fraction (assumed to be the "true" value) is plotted. The first part of the orbit (i.e., over land, ground pixel 0–120) is dominated by irregular mid-level cloud fields. For pixels 120–180 (approximatively over water, mediterranean basin) we find an homogeneous low cloud structure, until the equator is crossed and strong convective motion is dominant. The last part of the orbit (pixels 280–470) is located over water, in the persistent cloud system of Benguela gulf. Overall, ROCINN tends to underestimate CTHs with respect to SNGome (in Table 5 the statistics of the four orbits are given). A negative bias of $-0.63 \pm 1.46 \, \mathrm{km}$ (Loyola et al., 2007) and, more recently, of $-0.44 \, \mathrm{km} \pm 1.26 \, \mathrm{km}$ (Loyola R. et al., 2010) have been found, where the same record of CTHs from GOME-1 and METEOSAT were compared. The difference likely arises from the assumption in the ROCINN forward model that a cloud is a perfect Lambertian reflector, hence not accounting for multiple scattering of light inside the cloud. Nevertheless, not surprisingly, the retrievals show a similar behavior along-track due to the physical principle both algorithms are based on.

4 Results

This section is devoted to the analysis of cloud top height derived from GOME-1 observations during the period from year 1996 throughout 2002, due to missing global coverage after June 2003. We consider zonal averages and inter-annual variations

5 from 70° North to South. The single pixel GOME-1 spatial resolution is $320 \times 40\,\text{km}^2$ and a total orbit swath of approximately $960\,\text{km}^2$. Global coverage is reached in 3 days. While the raw data are available with the nominal sampling, for the zonal analysis the data have been re-gridded with a latitudinal and longitudinal spacing of 1.5°.

4.1 Global geographical analysis

10 We focus on geographical cloud top height distributions. Our aim is to highlight regional trends and annual distributions. For this purpose, the year 2001 is plotted for the four seasons in Fig. 7. The maps have been B-spline smoothed for visualization purposes after a pixel-counted average of daily composites. However, the ungridded retrievals are available as original data at IUP Bremen website (http://www.iup.uni-bremen.de/

15 ~sciaproc/SNGome/). In fact the main features of global cloudiness are already known and have been studied by other satellite groups. Nevertheless is it worth to mention that, in the presented maps, some world regions over ocean (and sometimes over parts of the coast) are characterized by specific cloud systems. A cloud system may be represented by one or several interacting cloud structures, hence we expect to be

20 able to detect some of them (i.e., water clouds) on a global scale.

Namely, over North Atlantic at mid-latitudes the "extra tropical cyclones" form in the late autumn through winter months and they can reach altitudes of ≈9 km. Such cloud systems are detected by SNGome. Especially the seasonality of the monsoon (stretching from Indochina to the Arabian Sea) is well pictured, together with the appearance

25 of the typhoons' cloud structures in the late summer and in the autumn in the far east region bordered, from the north side, by Japan and Taiwan Island from the south. The habitual cloud structures, termed "close convective cells", can be seen over south

Pacific, close to south Peruvian and Chilean coast. Their accumulation is mainly due to the cold Humboldt sea current, the high mountainous coast and winds from the Andes. They reach 2.5–3 km, rarely exceeding such altitudes. This region resembles the Benguela region, situated over south Atlantic, where cloud cells formation is mainly

5   due to the cold sea current and the warm winds from the continent. Another feature is the season-conditioned cloudiness over the Caribbean sea, where hurricanes are observed in the late summer and in the autumn.

In Fig. 8 we present zonally averaged seasonal vertical distributions of relative cloud amount for the year 2001 for the same data in Fig. 7. Data are normalized in a way

10   that for each latitude belt (2° increment) the sum of all CTHs is equal to 100 %. Cloud altitudes below 1.5 km are not appreciably detected by SNGome, therefore pointing out the issue of improving low atmosphere modeling in the theory. The seasonality is again well reproduced and the structure of the ITCZ with high clouds near the tropopause is depicted. In Stubenrauch et al. (2010) (p. 7207, Fig. 8) datasets from CALIPSO, AIRS

15   and the radar-lidar GEOPROF are compared for years 2007–2008, boreal winter and summer, and similar plots are presented. Notwithstanding the different temporal coverage, we observe a similar shift of the maximum around the equator. This maximum is placed by SNGome lower than CALIPSO and GEOPROF, indicating lack of sensitivity to both thin and thick cirrus clouds.

20   As a further investigation, cloud distributions are analyzed with respect to season, hemisphere and underlying surface. Retrievals are binned with 0.5 km spacing, normalized to the total number of counted cloudy pixels and plotted in Fig. 9 and Fig. 11.

Since we plot cloud distributions with respect to northern seasons, the behavior in Fig. 9 is expected. From winter seasons, where more mid-level clouds are observed,

25   the response to an increased heating is to shift the mean mode toward higher values during spring and summer. Likewise the high peaks in boreal cold seasons have to be linked to austral warmer seasons. The disentanglement of the frequency distributions is plotted in Fig. 11. It is evident from Fig. 11a and c that cloud top heights over land follow one-mode narrow distributions, whereas in both hemisphere over water broader

and irregularly shaped distributions appear. In particular, in the Southern Hemisphere we find again the hallmark of the persistent low-level cloud structures which contribute to the first modes, as seen in Fig. 11d.

Moreover, analytical functions were fitted to the normalized seasonal occurrences of Fig. 9 using a non-linear least-squares approach with two parameters and 95% confidence interval. Since the original data are clearly left skewed, thus non gaussian, a fit has been carried out with two type of popular distributions: log-normal and gamma. In a recent study (de la Torre Juárez et al., 2011) the authors explored the dependency of analytical PDFs on different spatial domains (defined as "pixels" with side length L) of cloud properties such as liquid water path and droplet effective radius. They found that the best descriptions are given by gamma distributions for scales $L > 100$ km, and by log-normal distributions otherwise. Our results for cloud top height are compatible with their findings, given the coarse spatial resolution of GOME-1 (i.e., $L \approx 110$ km). In Fig. 10 we show the seasonal fit to the gamma function, that has been found to be the best descriptor for the mono-modal CTH distribution for summer and autumn. Deviations from the analytical functions reveal regional features (highlighted in the disentangled histograms of Fig. 11), such as persistent cloud fields at 3–5 km in the Southern Hemisphere and the tropopause height at ≈ 13 km. If the second mode in winter and spring is looked for, a weighted sum of PDFs and four parameters are needed. In Table 6 the parameter pairs (a, b) are given for the four seasons of Fig. 10. They have been found fitting the gamma PDF, defined as

$$f(x|a,b) = \frac{1}{b^a \, \Gamma(a)} x^{a-1} e^{\frac{x}{b}}.$$ (9)

4.2 Zonal analysis

Average plots of cloud top height over years minimize the influence of short-time variations, nevertheless in Fig. 12, during the period 1997–1998, a shift in the maximum can be observed. If one considers cloud height as a proxy for atmosphere dynamics

and radiative processes, there might be a link to the development of El-Niño Southern Oscillation (ENSO). In 1997, when the ENSO had its first appearance within this record, a single maximum of zonal CTH at ≈ 9.3 km was situated in the belt $3°$ N–$10°$ N. As the ENSO developed further, reaching its maximum between November 1997 and April 1998, two distinct maxima of ≈ 9 km each were observed at $3°$ S and $10°$ N.

The Intertropical Convergence Zone (ITCZ), where the closure of the Hadley cell dominates circulation in a narrow belt close to the equator, was influenced by the E-W temperature asymmetry over the Pacific Ocean. The combination with the longitudinal Walker circulation and Earth rotation had the net effect to strengthen convection loops along the equator and to change heat distribution maps at the surface.

Cloud cover trends, retrieved in the O_2 A-band, have been found to be positively correlated with sea surface temperature (SST) (Wagner et al., 2005). Moreover, SST anomalies over Pacific Ocean have been found to be negative correlated with O_2 absorption (Wagner et al., 2008). Thus an increase in SST implies a shallower O_2 band, that is higher CTHs. This effect could be observed in ISCCP records during the ENSO episode back in 1987–1988: a change of SST of $2\,°C$ for temperatures $>26\,°C$ lowered cloud top pressure of ≈ 25 hpa (Bony et al., 1997), which means an increment in CTH of ≈ 3.6 km, therefore matching our retrievals, when the maxima of 1997 and 1998 at 3–$5°$ S are compared.

More recently, Larson and Hartmann (2003) numerically probed the response of tropical clouds and water vapor to SST anomaly. Their findings suggest that high cloud occurrence rises as compared to middle or low cloud ones. We focus on the tropical pacific region ($7.5°$ S–$10°$ N, $100°$ E–$280°$ E), as specified in Cess et al. (2001). High clouds (HC) are defined as clouds with $h > 6.5$ km, middle clouds (MC) with 3.2 km $< h < 6.5$ km and low clouds (LC) with $h < 3.2$ km (Stubenrauch et al., 2010) and in Fig. 13 their monthly relative averages are plotted. The seasonality, more pronounced in the HC, starting from mid 1998 onward until December 2002, is broken during the ENSO anomaly. In the time window February 1997–September 1998 the high cloud abundance never drops below 70 %, and middle and low cloud do not exhibit

Global cloud properties from GOME-1

L. Lelli et al.

Title Page

Abstract	Introduction
Conclusions	References
Tables	Figures

⏮ ⏭

◀ ▶

Back Close

Full Screen / Esc

Printer-friendly Version

Interactive Discussion

any periodicity as well. This confirms the role enhanced convection plays, linking the oceanic coupled system of non-dispersive Kelvin and off-equatorial non-dispersive Rossby waves (Dijkstra, 2002) with clouds in the tropics.

We present also the multi-annual global distribution of zonal mean cloud top height observed by GOME-1 in the boreal winter and summer (upper panel) with its difference (lower panel) in Fig. 14. Qualitatively, the CTH maximum is located in ITCZ region centered at 5° N–10° N in summer, while in winter the ITCZ moves southward, displacing the maximum at 5° S–7.5° S. In terms of hemispheric averages, winters clearly exhibit a lower CTHs at 22° N–25° N in the boreal belt, whereas 16° S–20° S in the austral belt. In opposite seasons (i.e., summer) this minimum vanishes and the average CTHs increase. These changes are related to changes in the atmospheric circulation over the annual cycle, that is, in the tropical Hadley cell and mid-latitude Ferrel cells and their intervening ITCZ (Mokhov and Schlesinger, 1993), as shown in the sinusoid in the lower panel of Fig. 14. For polar regions, the anomalous high peak during the austral winter can be related to a missing snow/ice screening in the algorithm. The increased reflectivity by bright surfaces is misinterpreted as high clouds. In Fig. 15 we plot the pixel-counted multi-annual average of daily composites of zonal CTH with 95 % confidence interval. A general hemispheric asymmetry is shown, linked to the abundance of land in the Northern Hemisphere, as compared to water predominance in the Southern.

Overall the global average cloud top height, derived from GOME-1 measurements for the years 1996–2002, is 7.0 ± 1.18 km (variance) in the belt of $\pm 70°$ latitude. This finding is in line with the value of 7.3 km derived from SCIAMACHY measurements for the years 2003–2006 (Kokhanovsky et al., 2011b).

5 Conclusions

We have presented properties of a seven-year global cloud dataset from the Global Ozone Monitoring Experiment GOME-1 using the semi-analytical cloud retrieval

Title Page

Abstract | Introduction

Conclusions | References

Tables | Figures

|◄ | ►|

◄ | ►

Back | Close

Full Screen / Esc

Printer-friendly Version

Interactive Discussion

algorithm SACURA, hereafter termed SNGome. The retrieval is based on optimal estimation approach applied to radiances around the 760 nm O_2 absorption A-band. Auxiliary data used in the calculation are the Minimum Lambert-Equivalent Reflectivity values from TEMIS and the cloud cover from OCRA-DLR, both derived from GOME-1 measurements. The retrieved properties are spherical cloud albedo (CA), cloud optical thickness (COT) and cloud top height (CTH), whose characterization has been the main focus of this study. In this way we aim at supporting GOME-1 ozone and trace gases retrievals as well as long-term trend analysis of global and regional cloudiness with joined datasets from SCIAMACHY and GOME-2. We have found that, even at the coarse spatial resolution of GOME-1 pixel, CTH retrieved values are quantitatively comparable to altitudes as derived by other independent algorithms and techniques. The reliability of the dataset for studies on a regional scale has been illustrated. A temporal correlation between CTHs and the El Niño Southern Oscillation (ENSO) anomaly has been observed and related to atmosphere dynamics. On the global scale, distinctive features of cloudiness are reproduced satisfyingly. We have presented PDFs of locally normalized mean of seasonal CTH, providing a statistical description for climate model parameterization. The average CTH for the seven-year record (1996–2002) has been found to be 7.0 ± 1.18 km in the belt of $\pm 70°$ latitude.

References

Bony, S., Lau, K.-M., and Sud, Y. C.: Sea Surface Temperature and Large-Scale Circulation Influences on Tropical Greenhouse Effect and Cloud Radiative Forcing, J. Climate, 10, 2055–2077, doi:10.1175/1520-0442(1997)010<2055:SSTALS>2.0.CO;2, 1997. 5006

Brühl, C. and Crutzen, P.: MPIC two-dimensional model, in: The Atmospheric Effect of Strato-spheric Aircraft, edited by: Prather, M. and Remsberg, E., pp. 103–104, NASA Ref. Publications, 1993. 4997

Burrows, J., Weber, M., Buchwitz, M., Rozanov, V., Ladstätter Weissenmayer, A., Richter, A., DeBeek, R., Hoogen, R., Bramstedt, K., Eichmann, K., Eisinger, M., and Perner, D.: The Global Ozone Monitoring Experiment (GOME): Mission Concept and First Scientific Results, J. Atmos. Sci., 56, 151–175, doi:10.1175/1520-0469(1999)056<0151:TGOMEG>2.0.CO;2, 1999. 4993

Burrows, J., Borrel, P., and Platt, U.: The Remote Sensing of Tropospheric Composition from Space, Springer Berlin Heidelberg, doi:10.1007/978-3-642-14791-3, 2011. 4994

Cess, R., Zhang, M., Wang, P., and Wielicki, B.: Cloud structure anomalies over the tropical Pacific during the 1997/98 El Niño, Geophys. Res. Lett., 28, 4547–4550, 2001. 5006

Deirmendjian, D.: Electromagnetic scattering on spherical polydispersions, Elsevier Scientific Publishing, New York, NY, 1969. 4998

de la Torre Juárez, M., Davis, A. B., and Fetzer, E. J.: Scale-by-scale analysis of probability distributions for global MODIS-AQUA cloud properties: how the large scale signature of turbulence may impact statistical analyses of clouds, Atmos. Chem. Phys., 11, 2893–2901, doi:10.5194/acp-11-2893-2011, 2011. 5005

Dijkstra, H.: Fluid Dynamics of El Niño Variability, Annu. Rev. Fluid Mechanics, 34, 531–558, doi:10.1146/annurev.fluid.34.090501.144936, 2002. 5007

Earth Resources Observation and Science (EROS, USGS) Center: The Shuttle Radar Topography Mission (SRTM), http://www.dgadv.com/srtm30/, 2000. 4997

Ferlay, N., Thieuleux, F., Cornet, C., Davis, A., Dubuisson, P., Ducos, F., Parol, F., Riédi, J., and Vanbauce, C.: Toward New Inferences about Cloud Structures from Multidirectional Measurements in the Oxygen A Band: Middle-of-Cloud Pressure and Cloud Geometrical Thickness from POLDER-3/PARASOL, J. Appl. Meteorol. Climatol., 49, 2492–2507, doi:10.1175/2010JAMC2550.1, 2010. 4994, 5001

Fischer, J. and Grassl, H.: Detection of cloud-top height from reflected radiances within the oxygen A band, part 1: Theoretical studies, J. Appl. Meteorol., 30, 1245–1259, 1991. 4993

Gottwald, M. and Bovensmann, H.: SCIAMACHY Exploring the Changing Earth's Atmosphere, Springer, Dordrecht, 2010. 4994

King, M.: Determination of the Scaled Optical Thickness of Clouds from Reflected Solar Radiation Measurements, J. Atmos. Sci., 44, 1734–1751, doi:10.1175/1520-

Global cloud properties from GOME-1

L. Lelli et al.

Title Page

Abstract	Introduction
Conclusions	References
Tables	Figures

|◄ | ►|

◄ | ►

Back | Close

Full Screen / Esc

Printer-friendly Version

Interactive Discussion

0469(1987)044<1734:DOTSOT>2.0.CO;2, 1987. 4996

Koelemeijer, R., de Haan, J., and Stammes, P.: A database of spectral surface reflectivity in the range 335–772 nm derived from 5.5 years of 0.5 observations, J. Geophys. Res., 108, 4070, http://www.temis.nl/data/ler.html, doi:10.1029/2002JD002429, 2003. 4995

Kokhanovsky, A.: Cloud Optics, Springer, Dordrecht, 2006. 4995

Kokhanovsky, A. A. and Nauss, T.: Reflection and transmission of solar light by clouds: asymptotic theory, Atmos. Chem. Phys., 6, 5537–5545, doi:10.5194/acp-6-5537-2006, 2006. 4994

Kokhanovsky, A. and Rozanov, V.: The physical parameterization of the top-of-atmosphere reflection function for a cloudy atmosphere–underlying surface system: the oxygen A-band case study, J. Quant. Spectr. Rad. Tran., 85, 35–55, doi:10.1016/S0022-4073(03)00193-6, 2004. 4994

Kokhanovsky, A., Rozanov, V., Zege, E., Bovensmann, H., and Burrows, J.: A semianalytical cloud retrieval algorithm using backscattered radiation in 0.4–2.4 µm spectral region, J. Geophys. Res., 108, 4008, doi:10.1029/2001JD001543, 2003. 4994, 4995

Kokhanovsky, A., Mayer, B., Rozanov, V., Wapler, K., Burrows, J., and Schumann, U.: The influence of broken cloudiness on cloud top height retrievals using nadir observations of backscattered solar radiation in the oxygen A-band, J. Quant. Spectr. Rad. Tran., 103, 460–477, doi:10.1016/j.jqsrt.2006.06.003, 2007a. 4994

Kokhanovsky, A., Mayer, B., von Hoyningen-Huene, W., Schmidt, S., and Pilewskie, P.: Retrieval of cloud spherical albedo from top-of-atmosphere reflectance measurements performed at a single observation angle, Atmos. Chem. Phys., 7, 3633–3637, doi:10.5194/acp-7-3633-2007, 2007b. 4997

Kokhanovsky, A., Nauss, T., Schreier, M., von Hoyningen-Huene, W., and Burrows, J.: The Intercomparison of Cloud Parameters Derived Using Multiple Satellite Instruments, Geoscience and Remote Sensing, IEEE Transactions on, 45, 195–200, doi:10.1109/TGRS.2006.885019, 2007c. 4995

Kokhanovsky, A., Platnick, S., and King, M.: Remote Sensing of Terrestrial Clouds from Space using Backscattering and Thermal Emission Techniques, in: The Remote Sensing of Tropospheric Composition from Space, edited by: Guzzi, R., Imboden, D., Lanzerotti, L., Platt, U., Burrows, J., Borrell, P., and Platt, U., Physics of Earth and Space Environments, pp. 231–257, Springer Berlin Heidelberg, doi:10.1007/978-3-642-14791-3_5, 2011a. 4994

Kokhanovsky, A., Vountas, M., and Burrows, J.: Global Distribution of Cloud Top Height as Retrieved from SCIAMACHY Onboard ENVISAT Spaceborne Observations, Remote Sens.,

Title Page

Abstract | Introduction

Conclusions | References

Tables | Figures

|◄ | ►|

◄ | ►

Back | Close

Full Screen / Esc

Printer-friendly Version

Interactive Discussion

3, 836–844, doi:10.3390/rs3050836, 2011b. 5007

Kuji, M. and Nakajima, T.: Retrieval of Cloud Geometrical Parameters Using Remote Sensing Data, in: 11th Conf. on Cloud Physics, p. JP1.7, Am. Meteorol. Soc., Ogden, UT, 2002. 4993

Kuze, A. and Chance, K.: Analysis of cloud top height and cloud coverage from satellites using the O_2 A and B bands, J. Geophys. Res., 99, 14481–14491, 1994. 4993

Larson, K. and Hartmann, D. L.: Interactions among Cloud, Water Vapor, Radiation, and Large-Scale Circulation in the Tropical Climate. Part I: Sensitivity to Uniform Sea Surface Temperature Changes, J. Climate, 16, 1425–1440, doi:10.1175/1520-0442-16.10.1425, 2003. 5006

Loyola, D.: Automatic cloud analysis from polar-orbiting satellites using neural network and data fusion techniques, in: IEEE International Geoscience and Remote Sensing Symposium, vol. 4, pp. 2530–2534, 2004. 4995, 5001

Loyola, D. and Ruppert, T.: A new PMD cloud-recognition algorithm for GOME, ESA Earth Observation Quarterly, 58, 45–47, 1998. 4995, 5002

Loyola, D., Werner, T., Yakov, L., Thomas, R., Peter, A., and Rainer, H.: Cloud Properties Derived From GOME/ERS-2 Backscatter Data for Trace Gas Retrieval, IEEE Transactions on Geoscience and Remote Sensing, 49, 2747–2758, doi:10.1109/TGRS.2007.901043, 2007. 4999, 5001, 5002

Loyola R., D. G., Thomas, W., Spurr, R., and Mayer, B.: Global patterns in daytime cloud properties derived from GOME backscatter UV-VIS measurements, Int. J. Remote Sens., 31, 4295–4318, doi:10.1080/01431160903246741, 2010. 5002

Marshak, A., Davis, A., Wiscombe, W., and Titov, G.: The verisimilitude of the Independent Pixel Approximation used in cloud remote sensing., Remote Sens. Environ., 52, 72–78, 1995. 4994

Mokhov, I. and Schlesinger, M.: Analysis of Global Cloudiness 1. Comparison of Meteor, Nimbus 7, and International Satellite Cloud Climatology Project (ISCCP) Satellite Data, J. Geophys. Res., 98(D7), 849–868, doi:10.1029/93JD00530, 1993. 5007

Nakajima, T. and King, M.: Determination of the Optical Thickness and Effective Particle Radius of Clouds from Reflected Solar Radiation Measurements. Part I: Theory, J. Atmos. Sci., 47, 1878–1893, doi:10.1175/1520-0469(1990)047<1878:DOTOTA>2.0.CO;2, 1990.

Poulsen, C. A., Watts, P. D., Thomas, G. E., Sayer, A. M., Siddans, R., Grainger, R. G., Lawrence, B. N., Campmany, E., Dean, S. M., and Arnold, C.: Cloud retrievals from satellite data using optimal estimation: evaluation and application to ATSR, Atmos. Meas. Tech. Discuss., 4, 2389–2431, doi:10.5194/amtd-4-2389-2011, 2011. 4999, 5000

Rozanov, V. and Kokhanovsky, A.: Semianalytical cloud retrieval algorithm as applied to the cloud top altitude and the cloud geometrical thickness determination from top-of-atmosphere reflectance measurements in the oxygen A band, J. Geophys. Res., 109, 4070, doi:10.1029/2003JD004104, 2004. 4993, 4994, 4996, 4997, 4998

5 Rozanov, V., Kokhanovsky, A., and Burrows, J.: The determination of cloud altitudes using GOME reflectance spectra: Multilayered cloud systems., IEEE Transactions on Geoscience and Remote Sensing, 42, 1009–1017, 2004. 5001

Rozanov, V., Kokhanovsky, A., Loyola, D., Siddans, R., Latter, B., Stevens, A., and Burrows, J.: Intercomparison of cloud top altitudes as derived using GOME and ATSR-2 instruments

10 onboard ERS-2, Remote Sens. Environ., 102, 186–193, 2006. 4998, 5001, 5002, 5018

Rozanov, V., Rozanov, A., Kokhanovsky, A., and Burrows, J.: SCIATRAN: Software package for the solution of forward and inverse vector radiative transfer problems, J. Quant. Spectr. Rad. Tran., preprint, 2011. 4998

Saiedy, F., Jacobowitz, H., and Wark, D. Q.: On Cloud-Top Determination from Gemini-5, J.

15 Atmos. Sci., 24, 63–69, doi:10.1175/1520-0469(1967)024<0063:OCTDFG>2.0.CO;2, 1967. 4993, 4994

Sayer, A. M., Poulsen, C. A., Arnold, C., Campmany, E., Dean, S., Ewen, G. B. L., Grainger, R. G., Lawrence, B. N., Siddans, R., Thomas, G. E., and Watts, P. D.: Global retrieval of ATSR cloud parameters and evaluation (GRAPE): dataset assessment, Atmos. Chem. Phys., 11,

20 3913–3936, doi:10.5194/acp-11-3913-2011, 2011. 4999, 5000, 5001

Sherwood, S., Chae, J., Minnis, P., and McGill, M.: Underestimation of deep convective cloud tops by thermal imagery, Geophys. Res. Lett., 31, L11102, doi:10.1029/2004GL019699, 2004. 5001

Stephens, G.: Cloud feedbacks in the climate system: A critical review, J. Climate, 18, 237–

25 273, doi:10.1175/JCLI-3243.1, 2005. 4992

Stricker, N. C. M., Hahne, A., Smith, D. L., Delderfield, J., Oliver, M. B., and Edwards, T.: ATSR-2: The evolution in its design from ERS-1 to ERS-2, ESA Bulletin, 1995. 4999

Stubenrauch, C. J., Cros, S., Guignard, A., and Lamquin, N.: A 6-year global cloud climatology from the Atmospheric InfraRed Sounder AIRS and a statistical analysis in synergy with

30 CALIPSO and CloudSat, Atmos. Chem. Phys., 10, 7197–7214, doi:10.5194/acp-10-7197-2010, 2010. 5004, 5006

Wagner, T., Beirle, S., Grzegorski, M., Sanghavi, S., and Platt, U.: El Niño induced anomalies in global data sets of total column precipitable water and cloud cover derived from GOME on

Global cloud properties from GOME-1

L. Lelli et al.

Title Page

Abstract	Introduction
Conclusions	References
Tables	Figures

|◄ | ►|

◄ | ►

Back | Close

Full Screen / Esc

Printer-friendly Version

Interactive Discussion

ERS-2, J. Geophys. Res., 110, D15104, doi:10.1029/2005JD005972, 2005. 5006

Wagner, T., Beirle, S., Deutschmann, T., Grzegorski, M., and Platt, U.: Dependence of cloud properties derived from spectrally resolved visible satellite observations on surface temperature, Atmos. Chem. Phys., 8, 2299–2312, doi:10.5194/acp-8-2299-2008, 2008. 5006

5 Yamamoto, G. and Wark, D.: Discussion of letter by A. Hanel: Determination of cloud altitude from a satellite, J. Geophys. Res., 66, 3596–3596, doi:10.1029/JZ066i010p03596, 1961. 4993

Global cloud properties from GOME-1

L. Lelli et al.

Global cloud properties from GOME-1

L. Lelli et al.

Table 1. GOME-1 instrument technical specifications.

Parameter	
Data availability	Jun 1995–today
	(No global coverage since Jun 2003)
Equator crossing	10:30 a.m. Local Time
Spectral coverage	237–794 nm
Spectral resolution	0.2–0.4 nm
Viewing geometry	nadir (across-track scan angle ±32°)
Ground pixel size	$320 \times 40\,km^2$ ($80 \times 40\,km^2$ narrow mode)
Swath width	$\approx 960\,km$
Polarization Measuring Device (PMD)	
Spectral coverage	3 p-PMD
	295–397 nm, 397–580 nm, 580–745 nm
Ground pixel size	$40 \times 20\,km^2$

Table 2. TEMIS minimum Lambert-equivalent reflectivity database specifications.

Parameter	
Data time window	Jun 1995–Dec 2000
Data aggregation	monthly
Spectral bins	335, 380, 416, 440, 463, 494.5
	555, 610, 670, 758, 772 nm
Spectral resolution	1 nm
Spatial resolution	1° × 1°

Full Screen / Esc

Printer-friendly Version

Interactive Discussion

Table 3. Location of the radar facilities with elevation above mean sea level and instrumentation (L = Lidar, M = millimeter-wave cloud radar, C = Ceilometer, CR = Cloud Radar).

Site	Latitude	Longitude	Elevation, m	Instrument
Chibolton	51.145° N	1.437° W	90	94 Ghz CR
SGP (Central)	36.605° N	97.485° W	320	L, M, C
NSA (Barrow)	71.323° N	156.616° W	8	L, M, C
TWP (Nauru)	0.521° S	166.616° E	7.1	L, M, C

Table 4. Cloud top height (km), correlation coefficient r and average bias (km) w.r.t. Radar for Figs. 4 and 5.

	deep (r)	shallow (r)	Bias (deep/shallow)
Radar	9.11	5.39	–
SNGome	8.11 (0.58)	6.13 (0.58)	$-1.00/0.74$
GRAPE	6.56 (0.51)	4.38 (0.84)	$-2.55/-1.01$

Table 5. Statistics for average values of all orbits in Rozanov et al. (2006) for three retrieval algorithms. Bias values are given w.r.t. SNGome.

	CTH (km) ± stdv (km)	Bias (km)
SNGome	5.99 ± 1.65	–
ATSR	5.68 ± 1.53	-0.38
ROCINN	5.35 ± 1.60	-0.66

Table 6. Parameters of the CTH fit to gamma distribution.

Season	a	b
DJF	3.95	1.61
MAM	4.38	1.59
JJA	4.13	1.67
SON	3.87	1.69

Table 7. Zonal average values and standard deviations (1-σ) of Cloud Fraction (CF), Cloud Top Height (CTH), Cloud Optical Thickness (COT) and spherical Cloud Albedo (CA) derived from GOME-1 measurements from June 1996 to December 2002.

Region	CF	CTH (km)	COT	CA
35° N–60° N	0.892 ± 0.185	6.65 ± 2.55	20.24 ± 22.24	0.632 ± 0.109
15° N–35° N	0.747 ± 0.291	7.57 ± 3.47	18.78 ± 20.06	0.623 ± 0.103
0° N–15° N	0.718 ± 0.298	9.01 ± 3.5	19.04 ± 19.8	0.629 ± 0.102
0° S–15° S	0.741 ± 0.294	8.19 ± 3.7	17.74 ± 17.2	0.617 ± 0.098
15° S–35° S	0.792 ± 0.261	6.73 ± 3.42	16.64 ± 18.66	0.596 ± 0.097
35° S–60° S	0.891 ± 0.181	6.13 ± 2.56	20.66 ± 26	0.628 ± 0.110
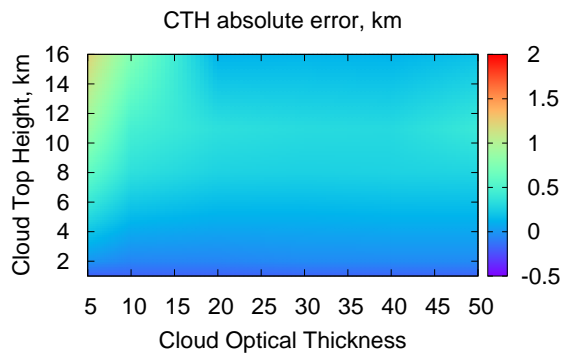
Fig. 1. Absolute error (in km) in the cloud top height retrieval with SNGome as function of cloud top height and optical thickness.

CTH absolute error, km
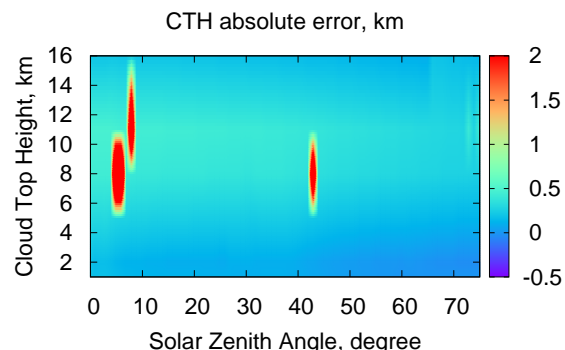
Fig. 2. As Fig. 1, but as a function of solar zenith angle in nadir view.
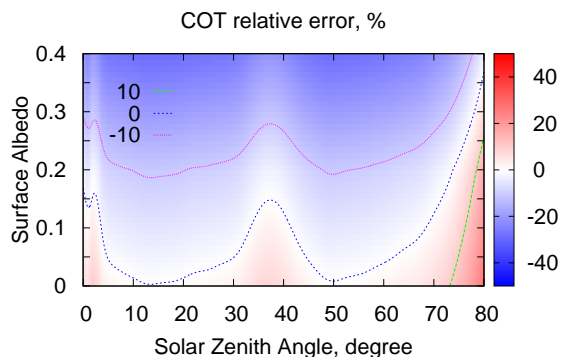
Fig. 3. Relative error (%) in cloud optical thickness retrieval as function of surface albedo and solar zenith angle. Input parameters: COT 20, CTH 5 km, geometrical thickness 1 km.
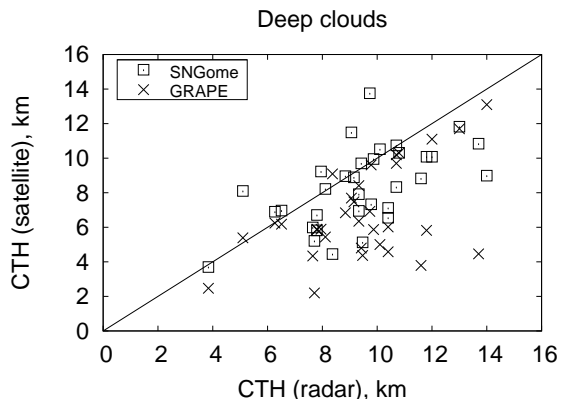
Fig. 4. Comparison between radar ground-based and satellite-based CTH retrievals for deep clouds.
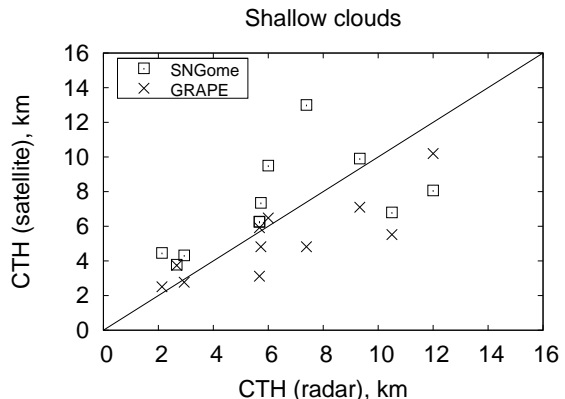
Fig. 5. As Fig. 4, but for shallow clouds.
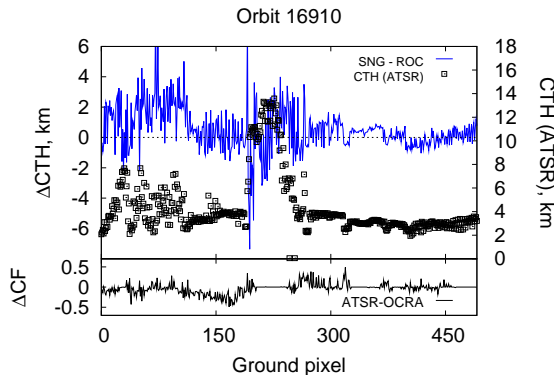
Fig. 6. Upper panel: along-track CTH difference between SNGome and ROCINN (blue curve, left y-axis) and ATSR cloud top heights (black squares, right y-axis) are plotted for the ERS-2 orbit 16910 (date 15 July 1998). Lower panel: cloud fraction difference between ATSR and OCRA.

Fig. 7. Maps of seasonal cloud top height for year 2001. Top to bottom: DJF, MAM, JJA, SON.
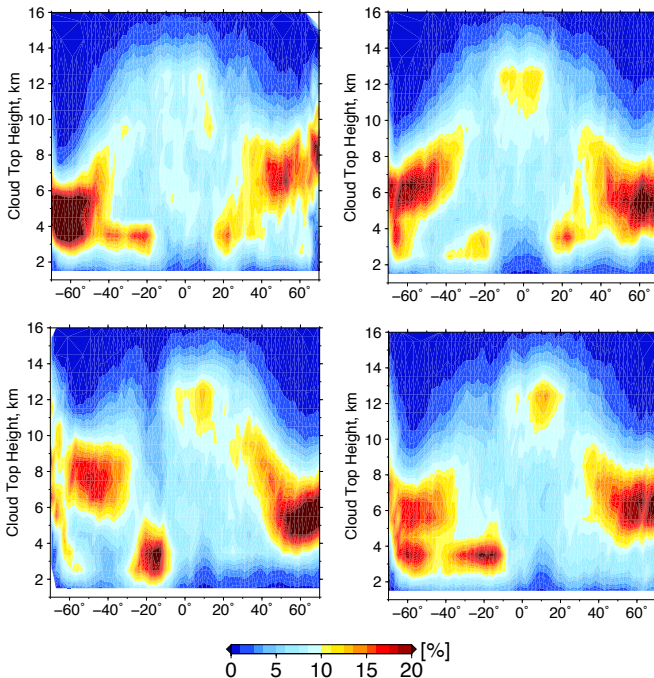
Fig. 8. Zonally averaged relative amount of seasonal cloud top height for year 2001. Top-left clockwise: DJF, MAM, JJA, SON.
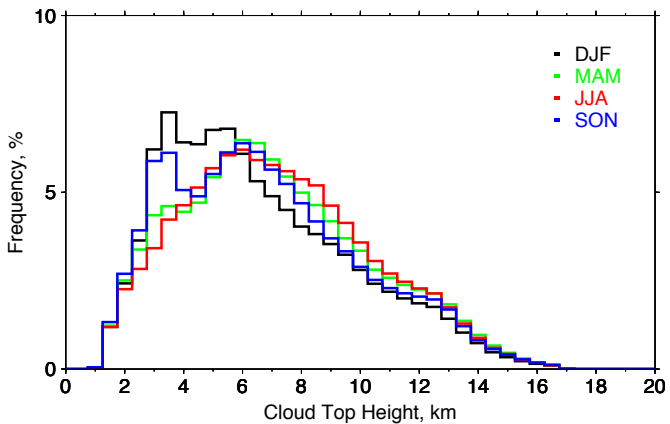
Fig. 9. Seasonal histogram of global cloud top height for 2001.
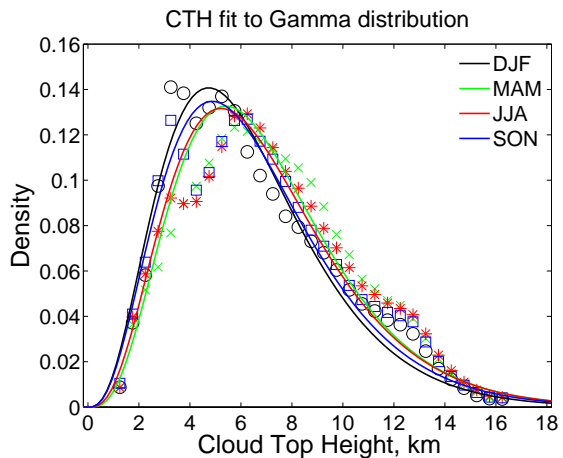
Fig. 10. Seasonal PDFs of Fig. 9 and their fit to Gamma distribution.
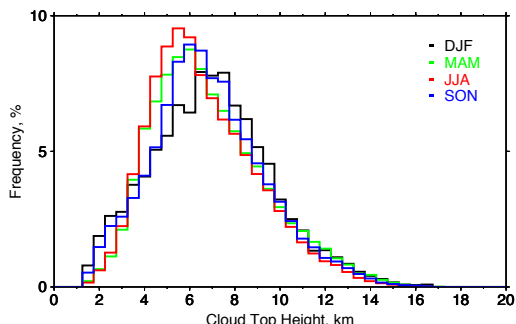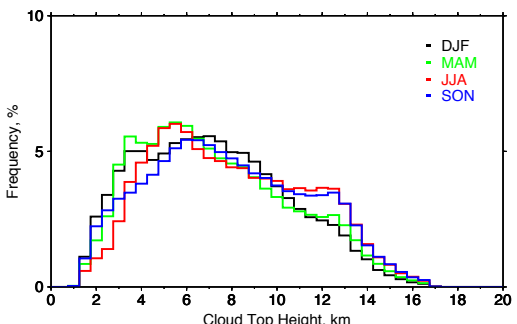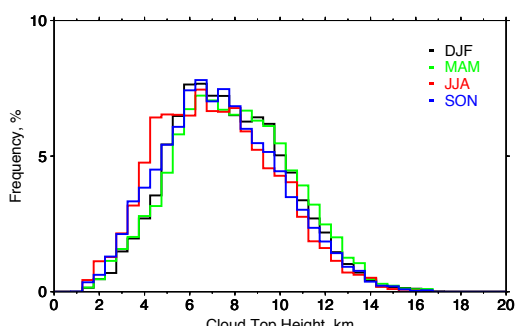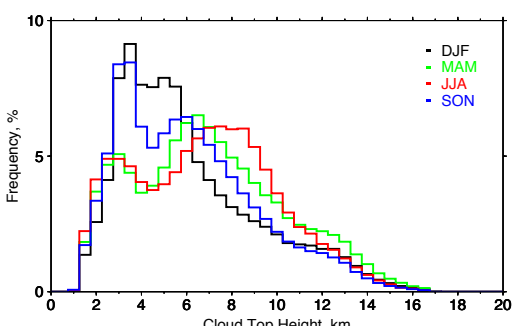
Fig. 11. Seasonal histograms of cloud top height for 2001. **(a)** over land, North; **(b)** over water, North; **(c)** over land, South; **(d)** over water, South.

Title Page

Abstract | Introduction

Conclusions | References

Tables | Figures

◄ | ►

◄ | ►

Back | Close

Full Screen / Esc

Printer-friendly Version

Interactive Discussion
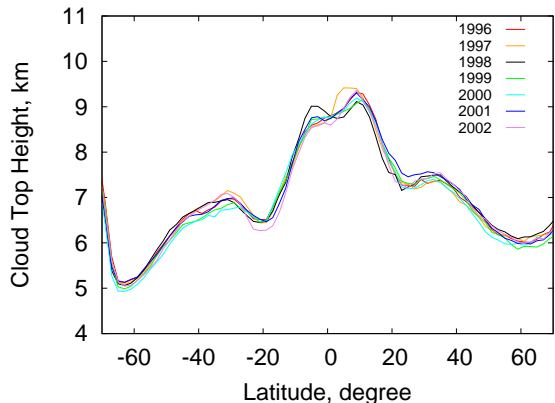
Fig. 12. Multiannual average cloud top heights from GOME-1.

Pacific Region (7.5°S – 10°N, 100°E – 280°E)
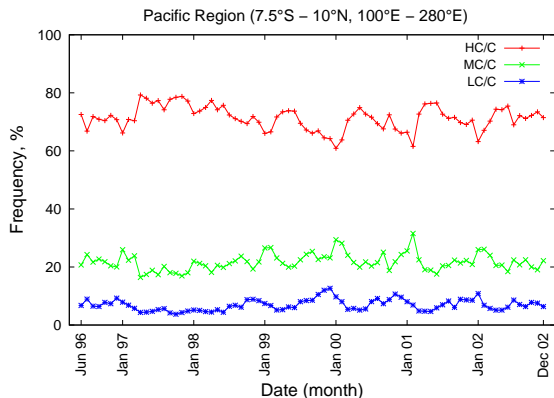
Fig. 13. Average relative cloud amount for low (LC), middle (MC) and high (HC) clouds in the Pacific Region where the El Niño anomaly (1997–1998) has been observed.
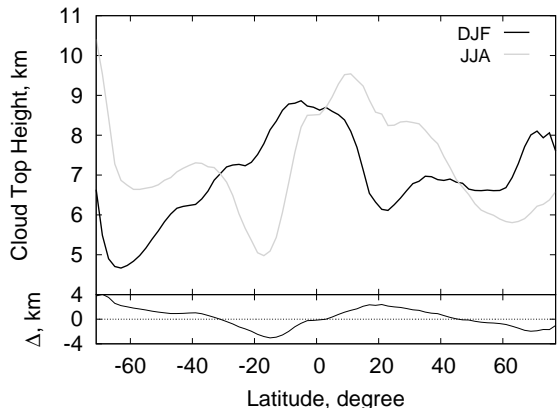
Fig. 14. Upper panel: multiannual average of cloud top height in boreal winter (DJF) and boreal summer (JJA). Lower panel: difference JJA–DJF.
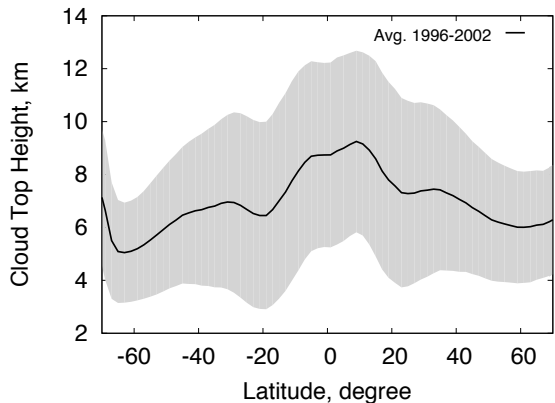
Fig. 15. Multiannual averaged cloud top height and 2-σ confidence interval.